JACS
JOURNAL OF THE AMERICAN CHEMICAL SOCIETY
pubs.acs.org/JACS
Article

Regulating Photocatalysis by Spin-State Manipulation of Cobalt in Covalent Organic Frameworks

Yun-Nan Gong,[⊥] Wenhui Zhong,[⊥] Yang Li, Yunze Qiu, Lirong Zheng, Jun Jiang,* and Hai-Long Jiang*

Cite This: *J. Am. Chem. Soc.* 2020, 142, 16723−16731

ABSTRACT: While catalysis is highly dependent on the electronic structure of the catalyst, the understanding of catalytic performance affected by electron spin regulation remains challenging and rare. Herein, we have developed a facile strategy to the manipulation of the cobalt spin state over covalent organic frameworks (COFs), COF-367-Co, by simply changing the oxidation state of Co centered in the porphyrin. Density functional theory (DFT) calculations together with experimental results confirm that Co^{II} and Co^{III} are embedded in COF-367 with $S = 1/2$ and 0 spin ground states, respectively. Remarkably, photocatalytic CO_2 reduction results indicate that COF-367-Co^{III} exhibits favorable activity and significantly enhanced selectivity to HCOOH, accordingly much reduced activity and selectivity to CO and CH_4, in sharp contrast to COF-367-Co^{II}. The results highlight that the spin-state transition of cobalt greatly regulates photocatalytic performance. Theoretical calculations further disclose that the presence of Co^{III} in COF-367-Co is preferable to the formation of HCOOH but detrimental to its further conversion, which clearly accounts for its distinctly different photocatalysis over COF-367-Co^{II}. To the best of our knowledge, this is the first report on regulating photocatalysis by spin state manipulation in COFs.

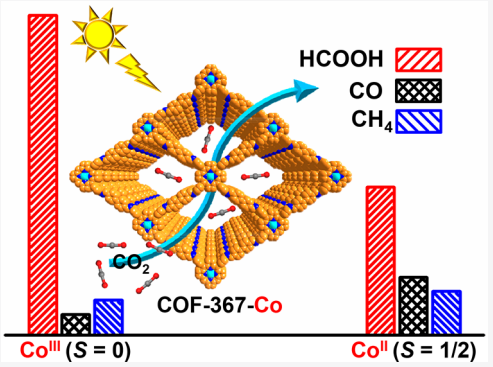

INTRODUCTION

With rapidly increasing combustion of fossil fuels, an energy crisis and environmental pollution are becoming global challenges.[1,2] Photocatalysis, achieving solar-to-chemical energy conversion, is recognized to be a very promising strategy to meeting these challenges.[3−6] Significantly, the development of suitable photocatalysts is extremely vital for the effective execution of this catalytic process. It is well-known that the performance of photocatalysts strongly depends on their intrinsic properties of electron states, such as spin state of transition metal sites.[7−9] Over the past few years, tremendous efforts have been made to the development of various strategies to modulate spin states of metal centers and thus further to improve their catalytic performance.[10−14] Among them, the change of metal oxidation state has been demonstrated to be a facile and effective strategy to overcome the complexity of catalytic system and tailor the overall electronic structure.[7,14] Nevertheless, it remains a great challenge to achieve such delicate control of electronic states in heterogeneous catalysts. To this end, the search for ideal catalyst models, which can stabilize active metal sites in different oxidation states without changing other structural parameters, to understand the inherent relationship between electronic state and photocatalytic performance is a highly desired target.

As a new class of crystalline porous materials, covalent organic frameworks (COFs),[15−19] which are constructed by linking molecular organic building units via covalent bonds, have shown great potential in photocatalysis.[20−23] Moreover, the periodic, well-defined and tailorable structures of COFs make them ideal candidates achieve in-depth insights into the structure−activity relationship.[24−31] Generally, the photocatalytic process includes light harvesting, electron−hole separation, and redox reaction, wherein charge separation plays a central role. Recently, a series of strategies, including the most accepted way of organic linker modification, have been developed to boost the charge separation of COFs and thus their photocatalytic performance.[32−36] However, to our knowledge, the investigations on electronic structure regulation of COFs on photocatalysis remain extremely rare.[32] Porphyrinic COFs involving highly conjugated π-electron macrocycles are promising in photocatalysis due to their excellent visible light harvesting ability.[37−39] Diverse metal ions can be readily implanted into the porphyrin centers to serve as active sites for photocatalysis. We deduce that the oxidation state modulation of metal ions centered in porphyrinic COFs might give rise to the transition of their spin states within the predetermined structure.

In this context, a representative porphyrinic COF, COF-367 involving cobalt-porphyrin, has been demonstrated to be an

Received: July 5, 2020
Published: September 7, 2020

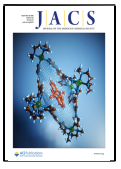

https://dx.doi.org/10.1021/jacs.0c07206
J. Am. Chem. Soc. 2020, 142, 16723−16731

ideal model based on density functional theory (DFT) simulations. The Co^{II} ions are implanted into the porphyrin units to afford COF-367-Co^{II}, in which the low spin state of Co^{II} (S = 1/2) is the ground state, 0.86 eV lower in energy than its high spin state (S = 3/2) (Table S1 of the Supporting Information, SI). By contrast, the ground state of Co^{III} in the COF-367-Co^{III} counterpart is in the absence of spin (S = 0), which is 0.15 and 0.41 eV lower in energy than those of its low (S = 1) and high (S = 2) spin states, respectively (Table S1). Therefore, the spin state of cobalt can be successfully modulated by simply changing its oxidation state in this ideal structure model of COF-367-Co (Scheme 1). Given that the ground spin state of Co is closely related to its catalytic performance, different catalytic behavior of COF-367-Co^{II} and COF-367-Co^{III} is therefore expected.

Scheme 1. Rational Fabrication of COF-367-Co Featuring Different Spin States of Co Ions toward Photocatalytic CO_2 Reduction

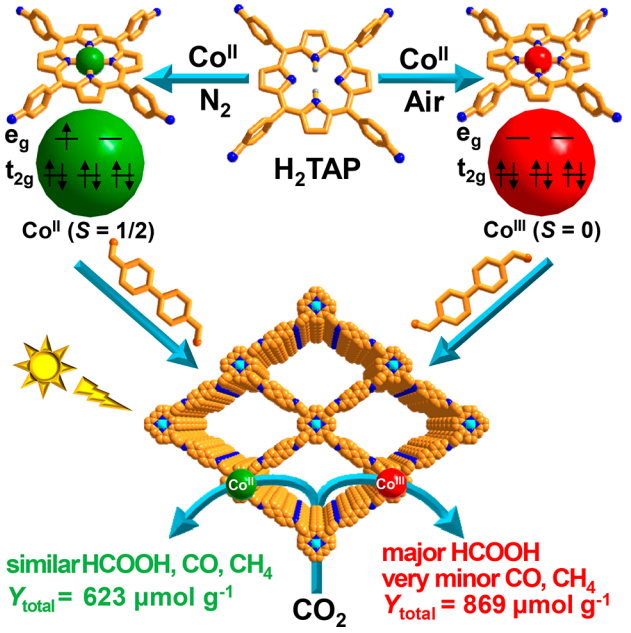

With the above in mind, COF-367-Co incorporating Co species in its porphyrin centers has been intentionally constructed. The Co^{II} center in the framework has been controllably oxidized to Co^{III} in the air without disturbing the overall structure (Scheme 1). Strikingly, photocatalytic results demonstrate that COF-367-Co^{III} (Co^{III}, S = 0) affords significantly higher activity and selectivity of CO_2 reduction to HCOOH, and lower selectivity to CO and CH_4, than COF-367-Co^{II} (Co^{II}, S = 1/2). DFT calculations unambiguously unveil that, in reference to COF-367-Co^{II}, the formation of HCOOH intermediate is preferred, whereas its further conversion is unfavorable by COF-367-Co^{III}, thus explaining the distinctly different photocatalytic activity and selectivity of the two COFs. As far as we know, this is the first report on spin-state transition in COFs for regulated photocatalysis.

MATERIALS AND METHODS

Materials and Equipment. All chemicals were obtained from commercial sources and used without further purification. Deionized water was produced by reversed osmosis (the specific resistance of 18.25 MΩ·cm) followed by ion-exchange and filtration (Cleaned Water Treatment Co., Ltd., Hefei). Powder X-ray diffraction patterns (XRD) were collected on a Japan Rigaku Miniflex 600 rotation anode X-ray diffractometer equipped with graphite monochromatized Cu Kα radiation (λ = 1.54 Å). Field-emission scanning electron microscopy (FE-SEM) was acquired on a Zeiss Supra 40 field emission scanning electron microanalyzer. Liquid-state UV−vis absorption spectra were recorded on a Shimadzu UV-2700 spectrophotometer. Solid-state UV−vis−NIR absorption spectra were obtained on a Shimadzu UV-3600 spectrophotometer and a white standard of $BaSO_4$ was used as a reference. Solid-state cross-polarization magic angle spinning nuclear magnetic resonance (^{13}C CP-MAS NMR) spectra were taken with a Bruker AVANCE III 400WB spectrometer. The gas sorption measurements were conducted using Micromeritics ASAP 2020 and MicrotracBEL BELSORP-Mas systems. The steady-state photoluminescence (PL) emission spectra were recorded on an LS-55 fluorescence spectrometer made by PerkinElmer. Electron paramagnetic resonance (EPR) spectra were collected on JEOL JES-FA200 EPR spectrometer. FT−IR spectra were recorded on Nicolet 6700 and Bruker Tensor 27 IR spectrometers, and samples were tableted with KBr as support. X-ray photoelectron spectroscopy (XPS) measurements were carried out on Kratos Axis Ultra DLD and ESCALAB 250 systems using monochromated Al Kα radiation as the excitation source. Gas chromatograph (GC) measurements were performed using a SHIMADZU GC-2014 instrument equipped with Porapak N (GS-Tek) and MOLSIEVE 13X (Agilent) packed columns, with a thermal conductivity detector (TCD) for H_2 and D_2 determinations, and flame ionization detector (FID) for CO and CH_4 determinations. The liquid products were analyzed using ion chromatography (CASTLE C1K-3K UPS) and ^{13}C nuclear magnetic resonance (NMR, Bruker AVANCE AV III 400) spectroscopy. The isotope of ^{13}C for CO and CH_4 was analyzed using mass spectrometry (HPR-20 QIC).

Synthesis of H_2TAP. The H_2TAP was synthesized according to the previous report with modifications as follows.[40] The mixture of acetic anhydride (12.0 mL) and propionic acid (300 mL) was refluxed with 4-nitrobenzaldehyde (11.0 g), then pyrrole (5.0 mL) was slowly added. After 30 min, the mixture was cooled down to room temperature. The precipitate was collected by filtration and washed with H_2O and methanol. Pyridine (80 mL) was refluxed with the resulting powder for 1 h. After cooling down to room temperature and freezing in the refrigerator overnight, the precipitate was collected by filtration and washed with acetone to give 5,10,15,20-Tetra(4-nitrophenyl)-porphyrin. The product (0.4 g) was dissolved in hydrochloric acid (50 mL) under N_2 atmosphere, then the $SnCl_2{\cdot}2H_2O$ (1.8 g) was added. The above mixture was heated at 75 °C for 0.5 h and then cooled down to 0 °C with an ice bath. The aqueous ammonia (25 mL) was slowly added. After stirring for 1 h, the resulting green product was collected by filtration, which was dissolved in 40 mL 5% NaOH aqueous solution. After stirring at room temperature for 0.5 h, the precipitate was collected by filtration and washed with water until the pH value of filtrate is about 7. The resulting powder was dried under vacuum at 60 °C for 12 h and then Soxhlet extracted with acetone (150 mL) for 24 h. Then, rotary evaporation of the solution followed by drying under vacuum afforded 5,10,15,20-tetra(4-aminophenyl)-porphyrin (H_2TAP) as blue crystals.

Synthesis of Co^{II}-TAP. Typically, H_2TAP (90 mg) was dissolved in $CHCl_3$ (4 mL), then a DMF solution (4 mL) of $Co(CH_3COO)_2{\cdot}4H_2O$ (85 mg) was added. The resulting mixture was heated at 100 °C for 16 h in N_2 atmosphere. After cooling down to room temperature, rotary evaporation of the solution followed by washing with water for six times gave dark purple solid, which was dispersed in 2 mL 10% $NaBH_4$ aqueous solution and stirred for 0.5 h. The precipitate was collected by filtration and dried under vacuum at 60 °C for 12 h to yield Co^{II}-TAP.

Synthesis of Co^{III}-TAP. Typically, H_2TAP (90 mg) was dissolved in $CHCl_3$ (4 mL), then a DMF solution (4 mL) of $CoCl_2{\cdot}6H_2O$ (85 mg) was added. The resulting mixture was heated at 100 °C in N_2 atmosphere. After 16 h, the reaction was changed to proceed in the air for 2 h, then the reaction mixture was cooled down to room temperature. Rotary evaporation of the solution followed by washing

https://dx.doi.org/10.1021/jacs.0c07206
J. Am. Chem. Soc. 2020, 142, 16723−16731

with water for six times gave dark purple solid, which was dried under vacuum at 60 °C for 12 h to yield Co^{III}-TAP.

Synthesis of COF-367-Co^{II}. A mixture of Co^{II}-TAP (18.0 mg), 4,4′-biphenyldicarboxaldehyde (BPDA, 15.6 mg), 1,2-dichlorobenzene (1.0 mL), ethanol (1.0 mL), 3-aminopropyltriethoxysilane (30 μL) and 6 M aqueous acetic acid (0.25 mL) was added into a Pyrex tube in 10 × 8 mm^2 (o.d × i.d), which was sonicated for 30 min. This mixture was flash frozen at 77 K (liquid N_2 bath). Then the tube was evacuated to an internal pressure of 50 mTorr and sealed off. The reaction proceeded at 120 °C for 72 h. After cooling down to room temperature, the dark purple product was collected by filtration and washed with acetone for 3 times, followed by soaking in acetone for 24 h. Finally, the product was evacuated at 150 °C for 12 h at 10^{-2} mTorr to yield the activated sample of COF-367-Co^{II}.

Synthesis of COF-367-Co^{III}. COF-367-Co^{III} was synthesized following the same procedures as COF-367-Co^{II} except for the addition of Co^{III}-TAP instead of Co^{II}-TAP.

Synthesis of COF-367. COF-367 was synthesized following the same procedures as COF-367-Co^{II} except for the addition of H_2TAP (15.0 mg) and BPDA (10.0 mg) respectively, instead of a mixture of Co^{II}-TAP and BPDA.

Synthesis of COF-366. COF-366 was synthesized following the same procedures as COF-367-Co^{II} except for the addition of H_2TAP (15.0 mg) and 1,4-benzenedicarboxaldehyde (BDA, 6.5 mg) respectively, instead of the mixture of Co^{II}-TAP and BPDA.

Synthesis of COF-366-Co^{II}. COF-366-Co^{II} was synthesized following the same procedures as COF-367-Co^{II} except for the addition of BDA (10.0 mg) instead of BPDA.

XAFS Measurements. The X-ray absorption fine structure (XAFS) spectra for the K-edge absorption of Co were collected at the beamline 1W1B station of the Beijing Synchrotron Radiation Facility (BSRF). The storage ring was operated at 2.5 GeV with an average current of 250 mA. Using Si(111) double-crystal monochromator and ionization chamber, the data were performed in a transmission mode for COF-367-Co^{II}, COF-367-Co^{III}, $Co(acac)_2$, $Co(acac)_3$, $CoCl_2$, and Co foil. All spectra were collected under ambient conditions.

Photocatalytic Performance Evolution. The CO_2 reduction reaction was performed in a 160 mL photoreactor (Perfect Light, Beijing). A mixture of photocatalyst (10 mg), acetonitrile (CH_3CN, 20 mL), and triethylamine (TEA, 2 mL) was added into the photoreactor. The reaction system was degassed with CO_2 to remove O_2 and other gases, followed by a 300 W Xe lamp (CEL-HXF300, CEAULICHT) irradiation with a 380 nm filter. The collected gaseous products were detected using GC. The liquid products were analyzed using ion chromatography and ^{13}C NMR spectroscopy.

Photoelectrochemical Measurements. Photocurrent measurements were carried out on a CHI 760E electrochemical workstation via a standard three-electrode system in 0.1 M Na_2SO_4 solution with a working electrode, a platinum plate as the counter electrode, and a saturated Ag/AgCl electrode as a reference electrode. A 300 W xenon lamp with a 380 nm filter was used as the light source. The COF-367, COF-367-Co^{II}, or COF-367-Co^{III} (5 mg) was dispersed into a solution of 10 μL 5 wt % Nafion and 0.5 mL ethanol. Then the resulting mixture (60 μL) was deposited onto the surface of the FTO plate with an area of 4 cm^2 and left in the air for drying to prepare the working electrode. Photoresponsive signals of the catalysts were recorded under chopped light at 0.6 V.

Electrochemical impedance spectroscopy (EIS) of COF-367, COF-367-Co^{II}, and COF-367-Co^{III}, and Mott−Schottky plots of COF-367-Co^{II} and COF-367-Co^{III} were performed on the Zahner Zennium electrochemical workstation via a standard three-electrode system in 0.1 M Na_2SO_4 solution, which contains a working electrode, a platinum plate as counter electrode, and a saturated Ag/AgCl electrode as a reference electrode. The catalyst (5 mg) was dispersed into a solution of 10 μL 5 wt % Nafion and 0.5 mL ethanol. Then the resulting mixture (30 μL) was deposited onto the surface of the glassy carbon (Φ = 3 cm) and left in the air for drying to prepare the working electrode. EIS measurement was carried out at −1.6 V in the dark. Mott−Schottky plots were recorded at frequencies of 500, 1000, and 1500 Hz, respectively.

EPR Measurements. To detect unpaired electron of Co ions in COF-367-Co^{II} and COF-367-Co^{III}, the EPR spectra of solid powder were measured at room temperature in the air. To investigate the mechanism behind the CO_2 photoreduction over COF-367-Co^{II} and COF-367-Co^{III}, the samples were prepared by suspending the pristine powder of COF-367-Co^{II} or COF-367-Co^{III} in a solution of TEA and CH_3CN. EPR measurements were conducted at 140 K under the N_2 atmosphere in a sealed homemade EPR tube under irradiation with a xenon lamp (λ > 380 nm) if necessary.

Computational Details. In the DFT calculations, although only a portion of the porphyrin ring is drawn to exhibit the configuration of the active center, we choose the whole porphyrin ring (H_2TAP) as the model. Theoretical calculations were performed at the Perdew−Burke−Ernzerhof (PBE) exchange functional level of density functional theory (DFT),[41] which has been widely used for N-doped carbon supported transition metal-catalyzed systems.[42] The 6-31G (d, p) basis set and Lanl08(f) were chosen for C, N, O, H, and Co atoms, respectively.[43] A polarizable continuum model using the Integral Equation Formalism model (IEFPCM) is used for the solvent effects.[44] Vibration frequency calculations have verified that all optimized geometries have no imaginary frequency while every transition state holds only a single imaginary frequency. Calculations of intrinsic reaction coordinates (IRC) confirmed that structures of transition states indeed connected two relevant minima. Electron density and partial density-of-states (DOS) were generated with the Multiwfn 3.3.9 program.[45] Gibbs free energies were computed and used to analyze the reaction mechanism. All calculations were performed with the Gaussian 09 software package.[46]

RESULTS AND DISCUSSION

The Co^{II}-TAP was prepared by the reaction of H_2TAP and $Co(CH_3COO)_2{\cdot}4H_2O$ under N_2 atmosphere. In contrast, the H_2TAP was metalated with $CoCl_2{\cdot}6H_2O$ under N_2 atmosphere, followed by spontaneous oxidation of Co^{II} in the air to give Co^{III}-TAP (Figure S1). UV−vis absorption spectrum of Co^{II}-TAP shows the maximum absorption at 430 nm, presenting a significant blue shift of 23 nm compared with Co^{III}-TAP, revealing the formation of different oxidation states for Co species (Figure 1a).[47] The assembly of COF-367-Co^{II} and COF-367-Co^{III} were completed by the Schiff base reaction between BPDA and Co^{II}-TAP/Co^{III}-TAP at 120 °C in mixed solvents (see the Materials and Methods). Powder XRD patterns of both

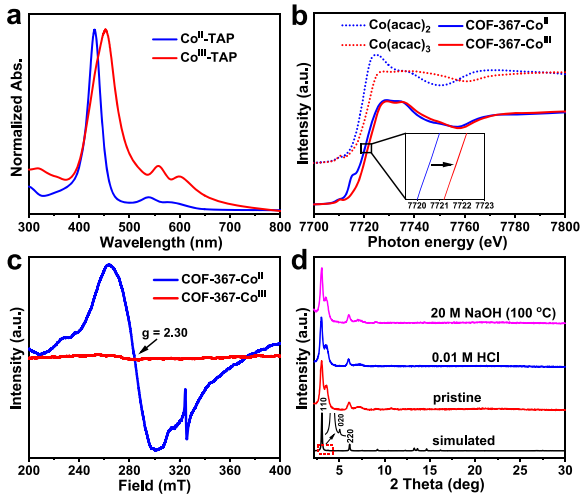

Figure 1. (a) UV−vis spectra of Co^{II}-TAP and Co^{III}-TAP. (b) The Co K-edge XANES spectra of COF-367-Co^{II}, COF-367-Co^{III}, $Co(acac)_2$, and $Co(acac)_3$. (c) EPR spectra of COF-367-Co^{II} and COF-367-Co^{III}. (d) Powder XRD patterns of COF-367-Co^{III} after treatment in 0.01 M HCl and 20 M NaOH for 12 h.

https://dx.doi.org/10.1021/jacs.0c07206
J. Am. Chem. Soc. 2020, 142, 16723−16731

COFs are in good agreement with that of simulated COF-367-Co^{II} (Figure S2),[48] supporting the successful formation of the expected structures. This can be supported by the FT−IR spectra, in which the characteristic imine stretching vibration band at 1622 cm^{-1} suggests the successful amine-aldehyde condensation to imine linkages (Figures S3 and S4).[48,49] The SEM images of COF-367-Co^{II} and COF-367-Co^{III} show similar rectangular rod-shaped morphology with ∼100 nm in length (Figures S5 and S6). XAFS measurements have been carried out to detect the evolution of Co oxidation state of COF-367-Co^{II} and COF-367-Co^{III} with $Co(acac)_2$ and $Co(acac)_3$ references. From the Co K-edge X-ray absorption near-edge structure (XANES) spectra, compared to COF-367-Co^{II}, the absorption edge of COF-367-Co^{III} noticeably shifts to a higher energy side, suggesting the increased Co oxidation state (Figure 1b).[50] To further verify the cobalt oxidation state in both COFs, XPS spectra have been collected. The Co $2p_{1/2}$-$2p_{3/2}$ spin−orbit level energy spacing is 16 eV for COF-367-Co^{II}, while it is 15 eV for COF-367-Co^{III}, suggesting the +2 and +3 oxidation states of Co species in COF-367-Co^{II} and COF-367-Co^{III}, respectively (Figures S7 and S8).[51,52] In fact, a clear Cl 2p signal peak at 197.3 eV can be observed in COF-367-Co^{III}, which might be responsible for charge balance in the overall framework (Figure S9). The Fourier transform-extended X-ray absorption fine structure (FT-EXAFS) spectrum of COF-367-Co^{III} exhibits one main peak at about 1.56 Å corresponding to the Co−N bond, whereas no Co−Cl peak (∼2.02 Å) can be found, implying the free Cl^- within COF-367-Co^{III} (Figure S10). EPR measurements were further conducted to obtain the information on unpaired electron of Co ions in the COFs (Figure 1c). The EPR spectrum of COF-367-Co^{II} shows a strong signal at g = 2.30, while this signal disappears in that of COF-367-Co^{III}, suggesting that unpaired electron exists in COF-367-Co^{II} only. All these results well support the original DFT calculations that Co^{II} and Co^{III} are incorporated in COF-367-Co with S = 1/2 and 0 spin ground states, respectively (Table S1). In addition, COF-366, COF-366-Co^{II}, and COF-367 have been also synthesized by the similar Schiff base reaction (Figure S11).

The porous feature of COF-367, COF-367-Co^{II}, and COF-367-Co^{III} has been examined by N_2 sorption at 77 K, presenting similar Brunauer−Emmett−Teller (BET) surface areas of 442, 580, and 489 m^2/g, respectively, and almost the same pore size distributions (12 to 25 Å) (Figures S12−S14). Moreover, COF-367-Co^{II} and COF-367-Co^{III} demonstrate their exceptionally high stability under extreme conditions of 0.01 M HCl solution at room temperature and 20 M NaOH solution at 100 °C treatment for 12 h, as evidenced by well retained powder XRD patterns (Figures 1d and S15), placing them among the best chemical stability in all reported COFs. Solid-state UV−vis−NIR spectra of COF-367-Co^{II} and COF-367-Co^{III} exhibit their strong light-harvesting ability in the UV and visible light range, and relatively weak absorbance in the near-infrared region (Figures 2a and S16). Their band gap energies (E_g) are 1.03 and 1.10 eV, respectively, evaluated by the Kubelka−Munk (KM) method (Figures 2a and S16). To elucidate their semiconductor character and possibility for photocatalysis, Mott−Schottky measurements of COF-367-Co^{II} and COF-367-Co^{III} have been performed with the frequencies of 500, 1000, and 1500 Hz. All positive slopes of the C^{2-} values (vs applied potentials) of them show the character of an n-type semiconductor.[37] The flat bands are determined from the intersections of ∼ −1.16 and ∼ −1.04 V vs Ag/AgCl (i.e., −0.96 and −0.84 V vs NHE), respectively, which are equal to the conduction bands (LUMO). Therefore,

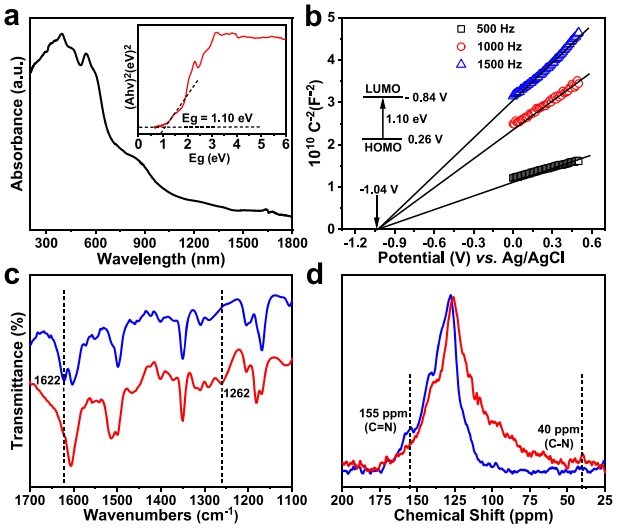

Figure 2. (a) UV−vis−NIR spectrum and tauc plot (inset) of COF-367-Co^{III} with imine group. (b) Mott−Schottky plots for COF-367-Co^{III} with imine group in 0.1 M Na_2SO_4 aqueous solution. Inset: the energy diagram of the HOMO and LUMO levels of COF-367-Co^{III}. (c) FT−IR and (d) ^{13}C CP-MAS NMR spectra of COF-367-Co^{III} before (blue) and after (red) the first light irradiation for 10 h.

their valence bands (HOMO) are accordingly calculated to be 0.07 and 0.26 V vs NHE, respectively (Figures 2b and S17). Obviously, both LUMO potentials are more negative compared with some typical photocatalytic products such as H_2 (0 V), HCOOH (0.58 V), CO (0.51 V), and CH_4 (0.24 V), all potentials are with reference to NHE, suggesting that they are theoretically feasible for photocatalytic H_2 production and CO_2 reduction.

Encouraged by the above results, photocatalytic CO_2 reduction over COF-367-Co^{II} and COF-367-Co^{III} has been carried out with CH_3CN as solvent (its high CO_2 solubility and possible cation-solvating property in favor of efficient electron transfer to CO_2) and TEA as the sacrificial electron donor under visible light irradiation. The reaction generates HCOOH, CO, CH_4, and H_2 products together. It is uncommon that the yield of HCOOH, CO, and CH_4 in relatively low but gradually increased rates within the first 10 h, followed by steadily high production rates (Figures S18−S20). Surprisingly, the H_2 generation rate remains stable in the whole reaction process (Figure S21). In order to understand this unusual phenomenon, FT−IR spectra, ^{13}C CP-MAS NMR spectra and CO_2 sorption isotherms were collected. The FT−IR spectra for both COF-367-Co^{II} and COF-367-Co^{III} exhibit the gradual disappearance of the imine C═N stretching band at 1622 cm^{-1}, while accordingly the appearance of a new peak at 1262 cm^{-1} assignable to C−N stretching vibration, along with increasing reaction time up to 10 h (Figures 2c, S22, and S23).[49] Moreover, the ^{13}C CP-MAS NMR spectra for COF-367-Co^{III} as a representative show that the imine carbon peak at 155 ppm completely disappears, accompanied by the appearance of a new peak of amine carbon at 40 ppm after light irradiation (Figure 2d).[49] Given the above results, it is believed that the imine linkages in both COFs are reduced to amine linkages by H_2 in the reaction process, revealing that the tandem reaction of photocatalytic H_2 production and imine hydrogenation takes place (Scheme S1). The structures, redox potentials, and morphology of COF-367-Co^{II} and COF-367-Co^{III} with amine linkages are similar to those with imine linkages (Table S2, Figures S24−S26). In addition, the tandem reaction

https://dx.doi.org/10.1021/jacs.0c07206
J. Am. Chem. Soc. 2020, 142, 16723−16731

can be also conducted with other COFs containing imine linkages such as COF-366, COF-366-Co^{II}, and COF-367, after which the hydrogenation of imine linkages is confirmed by FT−IR spectra (Figures S27−S29). The resultant COF-367-Co^{II} and COF-367-Co^{III} bearing amine groups display much higher CO_2 uptake (22.54 and 26.23 $cm^3\ g^{-1}$) than that of the same COFs with imine groups (9.77 and 12.05 $cm^3\ g^{-1}$) at 1 atm and 298 K (Figures S30 and S31). This amine-enhanced CO_2 adsorption capability might be responsible for the gradually improved activity of CO_2 photoreduction over both COFs in the very beginning 10 h.[39]

Next, we have systematically investigated the performance of photocatalytic CO_2 reduction over both COFs with amine groups. After 8 h of visible light irradiation, the HCOOH, CO, and CH_4 yields of COF-367-Co^{II} are 3.89 ± 0.74, 1.32 ± 0.15, and 1.02 ± 0.15 μmol (related to production rates of 48.6 ± 9.25, 16.5 ± 1.88, and 12.8 ± 1.88 $\mu mol\ g^{-1}\ h^{-1}$), respectively (Figure 3a). In sharp contrast, COF-367-Co^{III} demonstrates

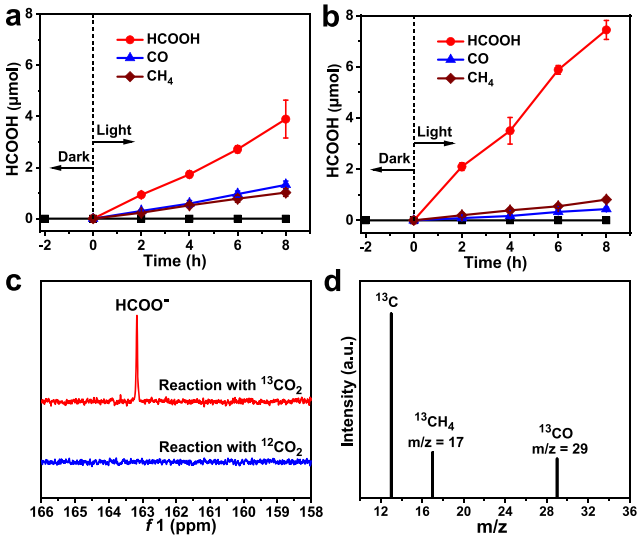

Figure 3. Amounts of HCOOH, CO, and CH_4 produced over (a) COF-367-Co^{II} and (b) COF-367-Co^{III} as a function of visible-light irradiation time. (c) ^{13}C NMR spectra for the product obtained from reaction over COF-367-Co^{III} with $^{13}CO_2$ instead of $^{12}CO_2$. (d) Mass spectrum for photocatalytic reduction of $^{13}CO_2$ to $^{13}CH_4$ and ^{13}CO using COF-367-Co^{III} as a photocatalyst.

significantly enhanced HCOOH production of 7.44 ± 0.37 μmol (93.0 ± 4.63 $\mu mol\ g^{-1}\ h^{-1}$), whereas reduced CO and CH_4 production of 0.44 ± 0.07 and 0.81 ± 0.09 μmol (5.5 ± 0.88 and 10.1 ± 1.12 $\mu mol\ g^{-1}\ h^{-1}$), respectively (Figure 3b). The electron consumption rate for CO_2 reduction can be evaluated based on the formula: $R_{electron}$ = (2Yield$_{HCOOH}$ + 2Yield$_{CO}$ + 8Yield$_{CH4}$)/0.01 g × 8 h, which are 233 and 278 $\mu mol\ g^{-1}\ h^{-1}$ for COF-367-Co^{II} and COF-367-Co^{III}, respectively. These results suggest that the cobalt spin-state transition in the two COFs accounts for their distinct photocatalytic activity and selectivity. In addition, the two COFs indeed present similarly low H_2 production rates of 3.7 ± 0.08 and 4.2 ± 0.2 $\mu mol\ g^{-1}\ h^{-1}$, respectively (Figure S21), demonstrating that most photogenerated electrons participate in CO_2 reduction with very high selectivities of 96.8 and 97.1% for COF-367-Co^{II} and COF-367-Co^{III}, respectively. For comparison, COF-367, Co^{II}-TAP, and Co^{III}-TAP for photocatalytic CO_2 reduction have also been evaluated under the identical conditions. No CO_2 reduction products can be detected for COF-367, highlighting the real active site of Co in COF-367-Co. Moreover, 0.36 ± 0.03 and 0.41 ± 0.04 μmol of HCOOH are produced only after 10 h over Co^{II}-TAP and Co^{III}-TAP catalysts, respectively (Figure S32), manifesting that the activity is greatly improved by assembling the Co-TAP complexes into COFs.

Additional control experiments demonstrate that no products can be detected in the absence of photocatalyst, CO_2, or light irradiation. To further confirm the origin of HCOOH, CO, and CH_4 products, the $^{13}CO_2$ isotope trace experiment is employed in the reaction. The ^{13}C NMR spectrum gives the HCOOH signal with peak at 163.2 ppm (Figures 3c and S33), and mass spectrum (MS) with the signal peaks at m/z = 29 (^{13}CO) and 17 ($^{13}CH_4$) can be observed (Figures 3d and S34), unambiguously verifying that the carbon source of HCOOH, CO and CH_4 products indeed comes from CO_2.[53,54] Moreover, the generated H_2 comes from water dissolved in CH_3CN or TEA, as proved by the D_2O introduction experiment (Figure S35). In addition, the catalytic stability of COF-367-Co^{III} was evaluated by recycling experiments, indicating the retained activity during the five consecutive runs (Figures S36−S38). UV−vis spectra and powder XRD profiles suggest structural integrity and no significant loss of crystallinity for both COFs after reaction (Figures S39−S41), demonstrating their excellent stability.

The possible mechanism behind the CO_2 photoreduction with COF-367-Co^{III} and COF-367-Co^{II} has been unveiled by EPR measurements (Figure S42). COF-367-Co^{II} shows a strong paramagnetic Co^{II} signal at g = 2.30 in the dark, which is reduced upon light irradiation, implying that Co^{II} is transformed to diamagnetic Co^{I}. By contrast, no ESR signal can be observed at g = 2.30 for COF-367-Co^{III} regardless of dark or irradiation conditions, hinting that the diamagnetic Co^{III} is possibly converted to diamagnetic Co^{I}.[55] With these results, it is proposed that, the TAP unit harvests visible light to generate charge-separated state, where electrons are transferred to the Co ions to reduce CO_2 in the presence of TEA as the sacrificial agent.

To elucidate the much higher photocatalytic CO_2 performance of COF-367-Co^{III} than COF-367-Co^{II}, photoelectrochemical measurements have been performed.[37] The COF-367-Co^{III} shows a higher photocurrent response than COF-367-Co^{II} (Figure S43), unveiling the better charge separation efficiency in the former. The EIS of COF-367-Co^{III} displays a smaller radius (Figure S44), inferring a lower charge-transfer resistance than COF-367-Co^{II}. Furthermore, PL intensity of COF-367-Co^{III} presents a larger degree of decrease than COF-367-Co^{II}, in comparison with the parent COF-367(Figure S45), further illustrating enhanced electron transfer after Co incorporation. The distinctly different photoelectrochemical properties among the samples above suggest charge separation efficiency follows the trend of COF-367-Co^{III} > COF-367-Co^{II} > COF-367, further accounting for their discriminative photocatalytic activity.

To further decode how the spin-state transition of cobalt affects the activity and selectivity, DFT calculations were conducted to gain insights into CO_2 adsorption and activation. The CO_2 molecule is first adsorbed onto COF-367-Co^{II} via the Co−O bonding with a bond length of 2.82 Å (Table S1). Its adsorption energy of 0.05 eV is reasonably weak for CO_2 adsorption. In stark contrast, the adsorption energy of CO_2 on COF-367-Co^{III} is more than doubled to be 0.11 eV, and the bond length of Co−O is reduced to 2.31 Å (Table S1), suggesting much stronger interaction than that on COF-367-

https://dx.doi.org/10.1021/jacs.0c07206
J. Am. Chem. Soc. 2020, 142, 16723−16731

Co^{II}. We have also witnessed different coupling strengths between atomic orbitals of Co-3d and O-2p of CO_2 in these two COFs from the partial density-of-states (PDOS) and overlap partial DOS (OPDOS) features (Figure S46a). From the orbital wave functions, the Co-3d_{xz} or Co-3d_{yz} coupling with O-2p in CO_2-adsorbed COF-367-Co^{II} is distinctly different from a strong overlap between O-2p and Co-3d_{z^2} in CO_2-adsorbed COF-367-Co^{III} (Figure 4a,b); and similarly, the stronger

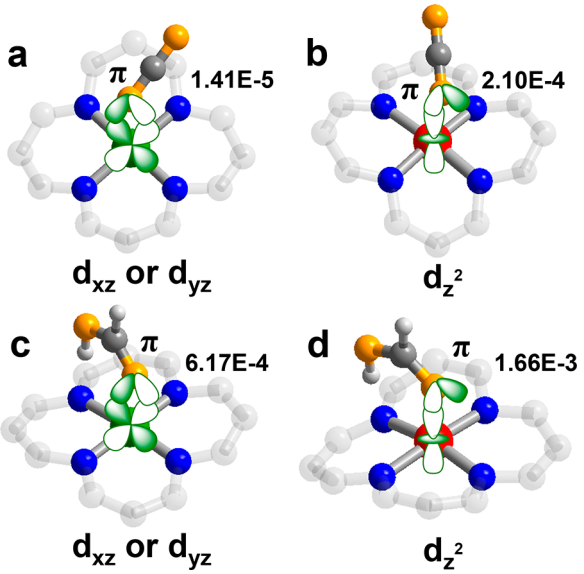

Figure 4. Different coupling modes of CO_2 and HCOOH interacting with Co site at different spin states for (a) CO_2-adsorbed COF-367-Co^{II}, (b) CO_2-adsorbed COF-367-Co^{III}, (c) HCOOH-interacted COF-367-Co^{II}, and (d) HCOOH-interacted COF-367-Co^{III}. The numerical values represent the corresponding OPDOS intensities.

HCOOH interaction occurs to COF-367-Co^{III} than COF-367-Co^{II} (Figure 4c,d, discussed far below). Therefore, the Co oxidation state (+2 or +3) remarkably affects the spin state, which in turn decides the electron distribution/orientation of Co-3d orbital (spin state), and significantly changes the interacting way of Co with CO_2 molecule. In COF-367-Co^{II} (S = 1/2), the Co-3d_{xz} or Co-3d_{yz} couples with O-2p. In contrast, the Co-3d_{z^2} couples with O-2p in COF-367-Co^{III} (S = 0). This difference accounts for the enhanced Co-3d/O-2p OPDOS coupling of CO_2-adsorbed COF-367-Co^{III} in reference to CO_2-adsorbed COF-367-Co^{II} (the integral areas of Co-3d/O-2p OPDOS: 2.10×10^{-4} vs 1.41×10^{-5} in Figure 4a,b), resulting in greatly promoted adsorption energy (0.11 vs. 0.05 eV) and implying improved catalytic activity.

Upon molecular adsorption, the CO_2 reduction to HCOOH could be catalyzed by COF-367-Co^{II} via two hydrogenation steps (Figure 5a). The first hydrogenation step occurs via a transition state TS1 by forming an O−H bond between oxygen in CO_2 and hydrogen, which is endothermic by 0.23 eV with an energy barrier of 0.65 eV. The second step is for the COOH to undergo an exothermic hydrogenation step (by 1.13 eV) with a barrier of 1.32 eV via the transition state TS2. This produces HCOOH, and is the rate-determining step for the overall reaction. From the configurations of transition sates (Figure 5a), we can see that CO_2 reduction by COF-367-Co^{II} relies on the synergistic effect of two active sites of N and Co, with the N site binding to one H atom while the Co site collecting the CO_2 molecule. In sharp contrast, using COF-367-Co^{III} catalyst, the

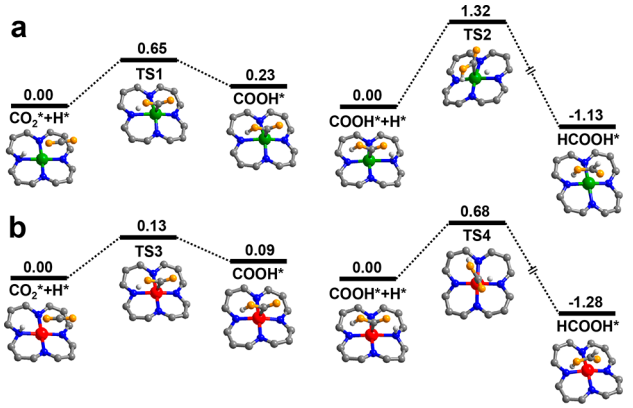

Figure 5. Calculated potential energy profile of CO_2 reduction reaction to HCOOH catalyzed by (a) COF-367-Co^{II} and (b) COF-367-Co^{III}. The Co(II), Co(III), C, N, O, and H atoms are shown in green, red, gray, blue, orange, and light gray, respectively.

barriers of the two consecutive hydrogenation steps are 0.13 and 0.68 eV via transition states of TS3 and TS4 (Figure 5b), which are much lower than those by COF-367-Co^{II}. The rate-determining step is noticeably lower with COF-367-Co^{III}, explaining its high activity and selectivity of CO_2 reduction to HCOOH in our experiment.

The generated HCOOH would subsequently be converted to CO or CH_4 products.[56−58] With COF-367-Co^{II} catalyst, the hydrogenation of HCOOH takes place through a transition state TS5 with a barrier of 0.54 eV (Figure S47a), which is endothermic by 0.15 eV. The formed $HC(OH)_2$ then undergoes an intramolecular dehydration reaction toward the intermediate of HCO through the transition state TS6 with a barrier of 0.97 eV (Figure S47a), as previously documented.[57] This process is exothermic by 0.15 eV and also the rate-determining step of the HCOOH reduction reaction. HCO is finally converted into CO by C−H bond rupture and CH_4 via subsequent hydrogenation.[58] In contrast, the barriers of the above two steps become 1.05 and 1.20 eV on COF-367-Co^{III} (Figure S47b). Inspiringly, the rate-determining step herein is noticeably lower on COF-367-Co^{II} than that of COF-367-Co^{III} (0.97 vs 1.20 eV), accounting again for the favorable HCOOH conversion to CO or CH_4 on COF-367-Co^{II}, in comparison to COF-367-Co^{III}, in experiments. In addition, different coupling strengths between atomic orbitals of Co-3d and O-2p of HCOOH in these two COFs are also perceived (Figure S46b). The differentiated HCOOH conversion ability can also be attributed to the different Co spin states. The Co oxidation state (+2 or +3) remarkably changes the spin state, which exhibits the electron distribution of Co-3d orbital, and thereby influences the interacting way/orientation of Co (Co-3d_{xz} or Co-3d_{yz} vs Co-3d_{z^2}) with O-2p orbital of HCOOH (Figure 4c,d). This results in different coupling strengths (6.17×10^{-4} vs 1.66×10^{-3}) as reflected by the integral areas of Co-3d/O-2p OPDOS, which visibly affects the HCOOH adsorption energy (0.47 vs 0.93 eV, Table S1) and its further conversion ability (0.97 vs 1.20 eV, Figure S47) on COF-367-Co^{II} and COF-367-Co^{III}, respectively, accordingly explaining their discriminative CO_2 photoreduction performance in experiments.

CONCLUSIONS

In summary, the COF-367-Co featuring Co centered in porphyrin units has been fabricated, of which the spin state of cobalt can be manipulated by regulating its oxidation state. The

https://dx.doi.org/10.1021/jacs.0c07206
J. Am. Chem. Soc. 2020, 142, 16723−16731

photocatalytic CO_2 reduction demonstrates that COF-367-Co^{III} (Co^{III}, $S = 0$) exhibits higher activity and remarkably higher selectivity to HCOOH product than COF-367-Co^{II} (Co^{II}, $S = 1/2$). For the first time, it demonstrates that the metal spin-state in COFs plays a crucial role in photocatalysis. All photoelectrochemical properties elucidate that COF-367-Co^{III} possesses higher charge separation efficiency than COF-367-Co^{II} and this accounts for the improved activity of the former. DFT calculations indicate that the lower energy barrier for the HCOOH formation and higher energy barrier for HCOOH further conversion to generate CO and CH_4 in COF-367-Co^{III}, than those of COF-367-Co^{II}. The calculation results well explain the distinctly different activity and selectivity of the two COFs and clarify how the spin-state transition affects the photocatalysis. This work provides a significant guideline to regulate the catalytic performance by rationally manipulating the spin state of metal centers.

■ ASSOCIATED CONTENT

Supporting Information

The Supporting Information is available free of charge at https://pubs.acs.org/doi/10.1021/jacs.0c07206.

Table S1, Energies of each system; Table S2, lattice parameters of COF-367-Co; Scheme S1, proposed scheme for the tandem reaction; Figure S1, UV−vis spectra; Figure S2, powder XRD patterns; Figure S3, FT−IR spectrum of COF-367-Co^{II}; Figure S4, FT−IR spectrum of COF-367-Co^{III}; Figure S5, SEM image of COF-367-Co^{II}; Figure S6, SEM image of COF-367-Co^{III}; Figure S7, XPS spectrum for the Co 2p of COF-367-Co^{II}; Figure S8, XPS spectrum for the Co 2p of COF-367-Co^{III}; Figure S9, XPS spectrum for the Cl 2p of COF-367-Co^{III}; Figure S10, FT-EXAFS spectra of COF-367-Co^{III}, $CoCl_2$, and Co foil; Figure S11, FT−IR spectra; Figure S12, N_2 sorption isotherms for COF-367; Figure 13, N_2 sorption isotherms for COF-367-Co^{II}; Figure S14, N_2 sorption isotherms for COF-367-Co^{III}; Figure S15, powder XRD patterns of COF-367-Co^{II}; Figure S16, UV−vis−NIR spectrum and tauc plot; Figure S17, Mott−Schottky plots for COF-367-Co^{II}; Figure S18, rate of HCOOH produced over COF-367-Co^{II} and COF-367-Co^{III}; Figure S19, rate of CO produced over COF-367-Co^{II} and COF-367-Co^{III}; Figure S20, rate of CH_4 produced over COF-367-Co^{II} and COF-367-Co^{III}; Figure S21, rate of H_2 produced over COF-367-Co^{II} and COF-367-Co^{III}; Figure S22, FT−IR spectra of COF-367-Co^{II}; Figure S23, FT−IR spectra of COF-367-Co^{III}; Figure S24, Rietveld refinement of COF-367-Co; Figure S25, UV−vis−NIR spectra and tauc plots; Figure S26, SEM images of COF-367-Co^{II} and COF-367-Co^{III}; Figure S27, FT−IR spectra of COF-366; Figure S28, FT−IR spectra of COF-366-Co^{II}; Figure S29, FT−IR spectra of COF-367; Figure S30, CO_2 adsorption curves; Figure S31, CO_2 adsorption curves; Figure S32, amounts of HCOOH; Figure S33, ^{13}C NMR spectra; Figure S34, mass spectra; Figure S35, GC analysis; Figure S36, rate of HCOOH produced; Figure S37, rate of CO produced; Figure S38, rate of CH_4 produced; Figure S39, UV−vis spectra; Figure S40, powder XRD patterns of COF-367-Co^{II}; Figure S41, powder XRD patterns of COF-367-Co^{III}; Figure S42, EPR spectra; Figure S43, photocurrent tests; Figure S44, EIS plots; Figure S45, PL spectra; Figure S46, PDOS and OPDOS density-of-states; Figure S47, calculated potential energy profile; and additional references (PDF)

■ AUTHOR INFORMATION

Corresponding Authors

Hai-Long Jiang − *Hefei National Laboratory for Physical Sciences at the Microscale, CAS Key Laboratory of Soft Matter Chemistry, Department of Chemistry, University of Science and Technology of China, Hefei, Anhui 230026, P. R. China;* orcid.org/0000-0002-2975-7977; Email: jianglab@ustc.edu.cn

Jun Jiang − *Hefei National Laboratory for Physical Sciences at the Microscale, CAS Key Laboratory of Soft Matter Chemistry, Department of Chemistry, University of Science and Technology of China, Hefei, Anhui 230026, P. R. China;* orcid.org/0000-0002-6116-5605; Email: jiangj1@ustc.edu.cn

Authors

Yun-Nan Gong − *Hefei National Laboratory for Physical Sciences at the Microscale, CAS Key Laboratory of Soft Matter Chemistry, Department of Chemistry, University of Science and Technology of China, Hefei, Anhui 230026, P. R. China; Key Laboratory of Jiangxi University for Functional Material Chemistry, College of Chemistry & Chemical Engineering, Gannan Normal University, Ganzhou 341000, P. R. China*

Wenhui Zhong − *School of Chemistry and Chemical Engineering, Qufu Normal University, Qufu, Shandong 273165, P. R. China;* orcid.org/0000-0003-1167-7220

Yang Li − *Hefei National Laboratory for Physical Sciences at the Microscale, CAS Key Laboratory of Soft Matter Chemistry, Department of Chemistry, University of Science and Technology of China, Hefei, Anhui 230026, P. R. China*

Yunze Qiu − *Hefei National Laboratory for Physical Sciences at the Microscale, CAS Key Laboratory of Soft Matter Chemistry, Department of Chemistry, University of Science and Technology of China, Hefei, Anhui 230026, P. R. China*

Lirong Zheng − *Beijing Synchrotron Radiation Facility, Institute of High Energy Physics, Chinese Academy of Sciences, Beijing 100049, P. R. China*

Complete contact information is available at: https://pubs.acs.org/10.1021/jacs.0c07206

Author Contributions

⊥These authors contributed equally.

Notes

The authors declare no competing financial interest.

■ ACKNOWLEDGMENTS

This work is supported by the NSFC (21725101, 21673213, 21871244, 21521001, 21963007), Fundamental Research Funds for the Central Universities (WK2060030029, WK2060190053) and DNL Cooperation Fund, Chinese Academy of Sciences (DNL201911). We thank the 1W1B station for XAFS measurement at the Beijing Synchrotron Radiation Facility (BSRF). The Supercomputing Center of University of Science and Technology of China is acknowledged for the computing resource.

■ REFERENCES

(1) Shindell, D.; Smith, C. J. Climate and Air-Quality Benefits of a Realistic Phase-Out of Fossil Fuels. *Nature* **2019**, *573*, 408−411.
(2) Gong, J.; Li, C.; Wasielewski, M. R. Advances in Solar Energy Conversion. *Chem. Soc. Rev.* **2019**, *48*, 1862−1864.

(3) Zhang, B.; Sun, L. Artificial Photosynthesis: Opportunities and Challenges of Molecular Catalysts. *Chem. Soc. Rev.* **2019**, *48*, 2216−2264.
(4) Rao, H.; Schmidt, L. C.; Bonin, J.; Robert, M. Visible-Light-Driven Methane Formation from CO_2 with a Molecular Iron Catalyst. *Nature* **2017**, *548*, 74−77.
(5) Wang, Z.; Li, C.; Domen, K. Recent Developments in Heterogeneous Photocatalysts for Solar-Driven Overall Water Splitting. *Chem. Soc. Rev.* **2019**, *48*, 2109−2125.
(6) Ran, J.; Jaroniec, M.; Qiao, S.-Z. Cocatalysts in Semiconductor-based Photocatalytic CO_2 Reduction: Achievements, Challenges, and Opportunities. *Adv. Mater.* **2018**, *30*, 1704649.
(7) Jiao, Y.; Sharpe, R.; Lim, T.; Niemantsverdriet, J. W. H.; Gracia, J. Photosystem II Acts as a Spin-Controlled Electron Gate during Oxygen Formation and Evolution. *J. Am. Chem. Soc.* **2017**, *139*, 16604−16608.
(8) Mtangi, W.; Kiran, V.; Fontanesi, C.; Naaman, R. Role of the Electron Spin Polarization in Water Splitting. *J. Phys. Chem. Lett.* **2015**, *6*, 4916−4922.
(9) Pan, L.; Ai, M.; Huang, C.; Yin, L.; Liu, X.; Zhang, R.; Wang, S.; Jiang, Z.; Zhang, X.; Zou, J.-J.; Mi, W. Manipulating Spin Polarization of Titanium Dioxide for Efficient Photocatalysis. *Nat. Commun.* **2020**, *11*, 418.
(10) Li, Q.-K.; Li, X.-F.; Zhang, G.; Jiang, J. Cooperative Spin Transition of Monodispersed FeN_3 Sites within Graphene Induced by CO Adsorption. *J. Am. Chem. Soc.* **2018**, *140*, 15149−15152.
(11) Tong, Y.; Guo, Y.; Chen, P.; Liu, H.; Zhang, M.; Zhang, L.; Yan, W.; Chu, W.; Wu, C.; Xie, Y. Spin-State Regulation of Perovskite Cobaltite to Realize Enhanced Oxygen Evolution Activity. *Chem.* **2017**, *3*, 812−821.
(12) Carmeli, I.; Kumar, K. S.; Heifler, O.; Carmeli, C.; Naaman, R. Spin Selectivity in Electron Transfer in Photosystem I. *Angew. Chem., Int. Ed.* **2014**, *53*, 8953−8958.
(13) Sun, S.; Shen, G.; Jiang, J.; Mi, W.; Liu, X.; Pan, L.; Zhang, X.; Zou, J.-J. Boosting Oxygen Evolution Kinetics by Mn-N-C Motifs with Tunable Spin State for Highly Efficient Solar-Driven Water Splitting. *Adv. Energy Mater.* **2019**, *9*, 1901505.
(14) Wei, C.; Feng, Z.; Scherer, G. G.; Barber, J.; Shao-Horn, Y.; Xu, Z. J. Cations in Octahedral Sites: A Descriptor for Oxygen Electrocatalysis on Transition-Metal Spinels. *Adv. Mater.* **2017**, *29*, 1606800.
(15) Waller, P. J.; Gándara, F.; Yaghi, O. M. Chemistry of Covalent Organic Frameworks. *Acc. Chem. Res.* **2015**, *48*, 3053−3063.
(16) Geng, K.; He, T.; Liu, R.; Dalapati, S.; Tan, K. T.; Li, Z.; Tao, S.; Gong, Y.; Jiang, Q.; Jiang, D. Covalent Organic Frameworks: Design, Synthesis, and Functions. *Chem. Rev.* **2020**, *120*, 8814−8933.
(17) Rodríguez-San-Miguel, D.; Zamora, F. Processing of Covalent Organic Frameworks: an Ingredient for a Material to Succeed. *Chem. Soc. Rev.* **2019**, *48*, 4375−4386.
(18) Yusran, Y.; Guan, X.; Li, H.; Fang, Q.; Qiu, S. Postsynthetic Functionalization of Covalent Organic Frameworks. *Natl. Sci. Rev.* **2020**, *7*, 170−190.
(19) Wang, Z.; Zhang, S.; Chen, Y.; Zhang, Z.; Ma, S. Covalent Organic Frameworks for Separation Applications. *Chem. Soc. Rev.* **2020**, *49*, 708−735.
(20) Wei, P.-F.; Qi, M.-Z.; Wang, Z.-P.; Ding, S.-Y.; Yu, W.; Liu, Q.; Wang, L.-K.; Wang, H.-Z.; An, W.-K.; Wang, W. Benzoxazole-Linked Ultrastable Covalent Organic Frameworks for Photocatalysis. *J. Am. Chem. Soc.* **2018**, *140*, 4623−4631.
(21) Kang, X.; Wu, X.; Han, X.; Yuan, C.; Liu, Y.; Cui, Y. Rational Synthesis of Interpenetrated 3D Covalent Organic Frameworks for Asymmetric Photocatalysis. *Chem. Sci.* **2020**, *11*, 1494−1502.
(22) Bhadra, M.; Kandambeth, S.; Sahoo, M. K.; Addicoat, M.; Balaraman, E.; Banerjee, R. Triazine Functionalized Porous Covalent Organic Framework for Photo-organocatalytic E-Z Isomerization of Olefins. *J. Am. Chem. Soc.* **2019**, *141*, 6152−6156.
(23) Wang, G.-B.; Li, S.; Yan, C.-X.; Zhu, F.-C.; Lin, Q.-Q.; Xie, K.-H.; Geng, Y.; Dong, Y.-B. Covalent Organic Frameworks: Emerging High-Performance Platforms for Efficient Photocatalytic Applications. *J. Mater. Chem. A* **2020**, *8*, 6957−6983.
(24) Ma, T.; Kapustin, E. A.; Yin, S. X.; Liang, L.; Zhou, Z.; Niu, J.; Li, L.-H.; Wang, Y.; Su, J.; Li, J.; Wang, X.; Wang, W. D.; Wang, W.; Sun, J.; Yaghi, O. M. Single-Crystal X-Ray Diffraction Structures of Covalent Organic Frameworks. *Science* **2018**, *361*, 48−52.
(25) Evans, A. M.; Parent, L. R.; Flanders, N. C.; Bisbey, R. P.; Vitaku, E.; Kirschner, M. S.; Schaller, R. D.; Chen, L. X.; Gianneschi, N. C.; Dichtel, W. R. Seeded Growth of Single-Crystal Two-Dimensional Covalent Organic Frameworks. *Science* **2018**, *361*, 52−57.
(26) Liang, R.-R.; Xu, S.-Q.; Zhang, L.; A, R.-H.; Chen, P.; Cui, F.-Z.; Qi, Q.-Y.; Sun, J.; Zhao, X. Rational Design of Crystalline Two-Dimensional Frameworks with Highly Complicated Topological Structures. *Nat. Commun.* **2019**, *10*, 4609.
(27) Huang, N.; Wang, P.; Addicoat, M. A.; Heine, T.; Jiang, D. Ionic Covalent Organic Frameworks: Design of a Charged Interface Aligned on 1D Channel Walls and Its Unusual Electrostatic Functions. *Angew. Chem., Int. Ed.* **2017**, *56*, 4982−4986.
(28) Han, X.; Zhang, J.; Huang, J.; Wu, X.; Yuan, D.; Liu, Y.; Cui, Y. Chiral Induction in Covalent Organic Frameworks. *Nat. Commun.* **2018**, *9*, 1294.
(29) Hu, Y.; Dunlap, N.; Wan, S.; Lu, S.; Huang, S.; Sellinger, I.; Ortiz, M.; Jin, Y.; Lee, S.; Zhang, W. Crystalline Lithium Imidazolate Covalent Organic Frameworks with High Li-ion Conductivity. *J. Am. Chem. Soc.* **2019**, *141*, 7518−7525.
(30) Ascherl, L.; Sick, T.; Margraf, J. T.; Lapidus, S. H.; Calik, M.; Hettstedt, C.; Karaghiosoff, K.; Döblinger, M.; Clark, T.; Chapman, K. W.; Auras, F.; Bein, T. Molecular Docking Sites Designed for the Generation of Highly Crystalline Covalent Organic Frameworks. *Nat. Chem.* **2016**, *8*, 310−316.
(31) Sun, T.; Wei, L.; Chen, Y.; Ma, Y.; Zhang, Y.-B. Atomic-Level Characterization of Dynamics of a 3D Covalent Organic Framework by Cryo-Electron Diffraction Tomography. *J. Am. Chem. Soc.* **2019**, *141*, 10962−10966.
(32) Vyas, V. S.; Haase, F.; Stegbauer, L.; Savasci, G.; Podjaski, F.; Ochsenfeld, C.; Lotsch, B. V. A Tunable Azine Covalent Organic Framework Platform for Visible Light-Induced Hydrogen Generation. *Nat. Commun.* **2015**, *6*, 8508.
(33) Chen, R.; Shi, J.-L.; Ma, Y.; Lin, G.; Lang, X.; Wang, C. Designed Synthesis of a 2D Porphyrin-Based sp^2 Carbon-Conjugated Covalent Organic Framework for Heterogeneous Photocatalysis. *Angew. Chem., Int. Ed.* **2019**, *58*, 6430−6434.
(34) Wang, H.; Qian, C.; Liu, J.; Zeng, Y.; Wang, D.; Zhou, W.; Gu, L.; Wu, H.; Liu, G.; Zhao, Y. Integrating Suitable Linkage of Covalent Organic Frameworks into Covalently Bridged Inorganic/Organic Hybrids toward Efficient Photocatalysis. *J. Am. Chem. Soc.* **2020**, *142*, 4862−4871.
(35) Zhang, M.; Lu, M.; Lang, Z.-L.; Liu, J.; Liu, M.; Chang, J.-N.; Li, L.-Y.; Shang, L.-J.; Wang, M.; Li, S.-L.; Lan, Y.-Q. Semiconductor/Covalent-Organic-Framework Z-Scheme Heterojunctions for Artificial Photosynthesis. *Angew. Chem., Int. Ed.* **2020**, *59*, 6500−6506.
(36) Guo, Z.; Zhang, Y.; Dong, Y.; Li, J.; Li, S.; Shao, P.; Feng, X.; Wang, B. Fast Ion Transport Pathway Provided by Polyethylene Glycol Confined in Covalent Organic Frameworks. *J. Am. Chem. Soc.* **2019**, *141*, 1923−1927.
(37) Lu, M.; Liu, J.; Li, Q.; Zhang, M.; Liu, M.; Wang, J.-L.; Yuan, D.-Q.; Lan, Y.-Q. Rational Design of Crystalline Covalent Organic Frameworks for Efficient CO_2 Photoreduction with H_2O. *Angew. Chem., Int. Ed.* **2019**, *58*, 12392−12397.
(38) Nagai, A.; Chen, X.; Feng, X.; Ding, X.; Guo, Z.; Jiang, D. A Squaraine-Linked Mesoporous Covalent Organic Framework. *Angew. Chem., Int. Ed.* **2013**, *52*, 3770−3774.
(39) Liu, W.; Li, X.; Wang, C.; Pan, H.; Liu, W.; Wang, K.; Zeng, Q.; Wang, R.; Jiang, J. A Scalable General Synthetic Approach toward Ultrathin Imine-linked Two-dimensional Covalent Organic Framework Nanosheets for Photocatalytic CO_2 Reduction. *J. Am. Chem. Soc.* **2019**, *141*, 17431−17440.
(40) Yuasa, M.; Oyaizu, K.; Yamaguchi, A.; Kuwakado, M. Micellar Cobaltporphyrin Nanorods in Alcohols. *J. Am. Chem. Soc.* **2004**, *126*, 11128−11129.

https://dx.doi.org/10.1021/jacs.0c07206
J. Am. Chem. Soc. 2020, 142, 16723−16731

(41) Perdew, J. P.; Burke, K.; Ernzerhof, M. Generalized Gradient Approximation Made Simple. *Phys. Rev. Lett.* **1996**, *77*, 3865−3868.
(42) Li, X. Y.; Cui, P.; Zhong, W. H.; Li, J.; Wang, X. J.; Wang, Z. W.; Jiang, J. Graphitic Carbon Nitride Supported Single-atom Catalysts for Efficient Oxygen Evolution Reaction. *Chem. Commun.* **2016**, *52*, 13233−13236.
(43) Roy, L. E.; Hay, P. J.; Martin, R. L. Revised Basis Sets for the LANL Effective Core Potentials. *J. Chem. Theory Comput.* **2008**, *4*, 1029−1031.
(44) Tomasi, J.; Mennucci, B.; Cammi, R. Quantum Mechanical Continuum Solvation Models. *Chem. Rev.* **2005**, *105*, 2999−3093.
(45) Lu, T.; Chen, F. Multiwfn: A Multifunctional Wavefunction Analyzer. *J. Comput. Chem.* **2012**, *33*, 580−592.
(46) Frisch, M. J.; Trucks, G. W.; Schlegel, H. B.; Scuseria, G. E.; Robb, M. A.; Cheeseman, J. R.; Scalmani, G.; Barone, V.; Mennucci, B.; Petersson, G. A.; Nakatsuji, H.; Caricato, M.; Li, X.; Hratchian, H. P.; Izmaylov, A. F.; Bloino, J.; Zheng, G.; Sonnenberg, J. L.; Hada, M.; Ehara, M.; Toyota, K.; Fukuda, R.; Hasegawa, J.; Ishida, M.; Nakajima, T.; Honda, Y.; Kitao, O.; Nakai, H.; Vreven, T.; Montgomery, J. A. J.; Peralta, J. E.; Ogliaro, F.; Bearpark, M.; Heyd, J. J.; Brothers, E.; Kudin, K. N.; Starov-Erov, V. N.; Keith, T.; Kobayashi, R.; Normand, J.; Raghavachari, K.; Rendell, A.; Burant, J. C.; Iyengar, S. S.; Tomasi, J.; Cossi, M.; Rega, N.; Millam, J. M.; Klene, M.; Knox, J. E.; Cross, J. B.; Bakken, V.; Adamo, C.; Jaramillo, J.; Gomperts, R.; Stratmann, R. E.; Yazyev, O.; Austin, A. J.; Cammi, R.; Pomelli, C.; Ochterski, J. W.; Martin, R. L.; Morokuma, K.; Zakrzewski, V. G.; Voth, G. A.; Salvador, P.; Dannenberg, J. J.; Dapprich, S.; Daniels, A. D.; Farkas, O.; Foresman, J. B.; Ortiz, J. V.; Cioslowski, J.; Fox, D. J. *Gaussian 09*, Revision D.01; Gaussian, Inc.: Wallingford, CT, 2009.
(47) Lin, Z.; Zhang, Z.-M.; Chen, Y.-S.; Lin, W. Highly Efficient Cooperative Catalysis by Co^{III}(Porphyrin) Pairs in Interpenetrating Metal-Organic Frameworks. *Angew. Chem., Int. Ed.* **2016**, *55*, 13739−13743.
(48) Lin, S.; Diercks, C. S.; Zhang, Y.-B.; Kornienko, N.; Nichols, E. M.; Zhao, Y.; Paris, A. R.; Kim, D.; Yang, P.; Yaghi, O. M.; Chang, C. J. Covalent Organic Frameworks Comprising Cobalt Porphyrins for Catalytic CO_2 Reduction in Water. *Science* **2015**, *349*, 1208−1213.
(49) Liu, H.; Chu, J.; Yin, Z.; Cai, X.; Zhuang, L.; Deng, H. Covalent Organic Frameworks Linked by Amine Bonding for Concerted Electrochemical Reduction of CO_2. *Chem.* **2018**, *4*, 1696−1709.
(50) Cao, L.; Luo, Q.; Liu, W.; Lin, Y.; Liu, X.; Cao, Y.; Zhang, W.; Wu, Y.; Yang, J.; Yao, T.; Wei, S. Identification of Single-Atom Active Sites in Carbon-Based Cobalt Catalysts During Electrocatalytic Hydrogen Evolution. *Nat. Catal.* **2019**, *2*, 134−141.
(51) Kent, C. A.; Concepcion, J. J.; Dares, C. J.; Torelli, D. A.; Rieth, A. J.; Miller, A. S.; Hoertz, P. G.; Meyer, T. J. Water Oxidation and Oxygen Monitoring by Cobalt-Modified Fluorine-Doped Tin Oxide Electrodes. *J. Am. Chem. Soc.* **2013**, *135*, 8432−8435.
(52) Zhu, M.; Chen, J.; Huang, L.; Ye, R.; Xu, J.; Han, Y.-F. Covalently Grafting Cobalt Porphyrin on Carbon Nanotube for Efficient CO_2 Electroreduction. *Angew. Chem., Int. Ed.* **2019**, *58*, 6595−6599.
(53) Zhang, H.; Wei, J.; Dong, J.; Liu, G.; Shi, L.; An, P.; Zhao, G.; Kong, J.; Wang, X.; Meng, X.; Zhang, J.; Ye, J. Efficient Visible-Light-Driven Carbon Dioxide Reduction by a Single-Atom Implanted Metal-Organic Framework. *Angew. Chem., Int. Ed.* **2016**, *55*, 14310−14314.
(54) Xu, H.-Q.; Hu, J.; Wang, D.; Li, Z.; Zhang, Q.; Luo, Y.; Yu, S.-H.; Jiang, H.-L. Visible-Light Photoreduction of CO_2 in a Metal-Organic Framework: Boosting Electron-Hole Separation via Electron Trap States. *J. Am. Chem. Soc.* **2015**, *137*, 13440−13443.
(55) Matsuoka, S.; Yamamoto, K.; Ogata, T.; Kusaba, M.; Nakashima, N.; Fujita, E.; Yanagida, S. Efficient and Selective Electron Mediation of Cobalt Complexes with Cyclam and Related Macrocycles in the *p*-Terphenyl-Catalyzed Photoreduction of Carbon Dioxide. *J. Am. Chem. Soc.* **1993**, *115*, 601−609.
(56) Wang, J.-Y.; Zhang, H.-X.; Jiang, K.; Cai, W.-B. From HCOOH to CO at Pd Electrodes: a Surface-Enhanced Infrared Spectroscopy Study. *J. Am. Chem. Soc.* **2011**, *133*, 14876−14879.
(57) Zhong, W.; Jiang, J. New Insight into CO Formation during HCOOH Oxidation on Pt(111): Intermolecular Dehydration of HCOOH Dimers. *J. Phys. Chem. C* **2015**, *119*, 19287−19296.
(58) Tian, X.; Wang, T.; Yang, Y.; Li, Y.-W.; Wang, J.; Jiao, H. About Copper Promotion in CH_4 Formation from CO Hydrogenation on Fe(100): A Density Functional Theory Study. *Appl. Catal., A* **2017**, *530*, 83−92.

https://dx.doi.org/10.1021/jacs.0c07206
J. Am. Chem. Soc. 2020, 142, 16723−16731